This document contains a post-print version of the paper

Unscented Kalman Filter for Vehicle State Estimation

authored by **S. Antonov, A. Fehn, and A. Kugi**

and published in *Vehicle System Dynamics.*

The content of this post-print version is identical to the published paper but without the publisher's final layout or copy editing. Please, scroll down for the article.

Link to original paper:

http://dx.doi.org/10.1080/00423114.2010.527994

Read more ACIN papers or get this document:

http://www.acin.tuwien.ac.at/literature

Contact:

Automation and Control Institute (ACIN)   Internet: www.acin.tuwien.ac.at
Vienna University of Technology   E-mail: office@acin.tuwien.ac.at
Gusshausstrasse 27-29/E376   Phone: +43 1 58801 37601
1040 Vienna, Austria   Fax: +43 1 58801 37699

Unscented Kalman Filter for Vehicle State Estimation

S. ANTONOV*†, A. FEHN‡, A. KUGI♯

† Dept. BEG-DP/EPF, Powertrain Systems, Bosch Engineering GmbH, Robert-Bosch-Allee 1,
74232 Abstatt, Germany

‡ Gustav-Freytag-Weg 27, 96450 Coburg, Germany

♯ Automation and Control Institute (ACIN), Vienna University of Technology, Gusshausstrasse 27–29 / E376,
1040 Vienna, Austria

Vehicle Dynamics Control (VDC) systems require the information about system variables, which cannot be directly measured, e.g., the wheel slip or the vehicle side-slip angle. This paper presents a new concept for the vehicle state estimation under assumption that the vehicle is equipped with the standard VDC sensors. It is proposed to utilize an Unscented Kalman Filter (UKF) for estimation purposes, since it is based on a numerically efficient nonlinear stochastic estimation technique. A planar two-track model is combined with the empiric Magic Formula in order to describe the vehicle and tire behavior. Moreover, an advanced vertical tire load calculation method is developed that additionally considers the vertical tire stiffness and increases the estimation accuracy. Experimental tests show the good accuracy and robustness of the designed vehicle state estimation concept.

Keywords: vehicle dynamics control, state estimation, unscented Kalman filter, UKF, vertical tire forces

1 Introduction

The first series Vehicle Dynamics Control (VDC) system was introduced by Robert Bosch GmbH in 1995 [1]. This system was designed to assist the driver during critical driving maneuvers. Thereby, the vehicle's skidding and spinning was prevented by means of selective braking of the individual wheels. In the past years VDC has shown a great contribution to crash avoidance [2, 3]. In series VDC systems the longitudinal and the lateral velocities of the vehicle as well as many other vehicle dynamics variables cannot be measured in a cost-efficient way. For this reason, an extensive research is performed for the estimation of the vehicle velocity, grip conditions, tire forces, and other relevant variables.

The latest publications are mainly concerned with different sensor configurations, diverse estimation techniques, as well as with the usage of various vehicle models. The well known industrial solutions typically rely on observers, which are based on heavily simplified dynamical vehicle models in combination with kinematic models. Normally, an additional switching or weighting logic is used for adaptation purposes. In this way, a model scheduling is performed depending on the tire slip conditions, see, e.g., [4–6]. In [7] a similar approach is applied for the planar two-track vehicle model with consideration of the load distribution and tire properties. In [8,9] an observer design based on Lyapunov's stability theory is proposed for the quarter vehicle model. The two-track vehicle model is utilized for various nonlinear observer design approaches in [10,11].

The main research activities in the field of vehicle dynamics estimation concentrate on the application of Kalman filter theory that is the most powerful tool for multi-sensor data fusion problems. The solutions combining a linear Kalman filter design for a one mass vehicle model with the fuzzy logic technique

---

*Corresponding author. e-mail: sergiy.antonov@de.bosch.com

have shown good performance at low computational effort [12, 13]. Several more sophisticated solutions were developed for more detailed vehicle models, mainly based on Kalman filter or Extended Kalman Filter (EKF) designs [14–21]. In [22] the two-track planar vehicle model is extended by a simple strategy to account for the vertical tire force calculation, the wheel dynamics, and the nonlinear tire model. The comparison of the introduced EKF and the high gain observer reveals that the EKF has better accuracy and robustness properties.

The main drawbacks of the EKF are the high computational effort for the calculation of the Jacobian matrices [22] as well as linearization errors, which force the usage of relatively small sampling times. For overcoming this hurdle, we propose to use the Unscented Kalman Filter (UKF), see, e.g., [23, 24], for the vehicle state estimation. The UKF induces computational costs comparable to the ones of EKF (cf. [24]) but does not require the linearization of the underlying model. The absence of the linearization error further allows us to execute the filter with lager sampling times.

In this paper, we will consider a passenger vehicle equipped with standard VDC sensors, i.e., the steering wheel angle, the four rotational wheel velocities, the yaw rate, and the lateral acceleration. We assume the propulsion and the braking torques of the wheels to be known as well, since they are estimated with acceptable accuracy in serial produced VDC systems. The planar two-track vehicle model is chosen as a basis for the filter design. Thereby, the pitch and the roll motion of the vehicle are not explicitly considered. This allows us to reduce the number of state variables and yields a lower computational effort. In contrast to the works [7, 18, 22], an advanced method for the vertical tire forces calculation is developed, which additionally accounts for the tire stiffness. The simplified empirical Magic Formula model [26, 27] is used for describing the tire/road interaction. The discretization of the complete vehicle model is performed by means of a truncated Lie-Taylor series. Afterwards, the performance of the augmented state UKF implementation is evaluated by means of real vehicle tests.

The structure of this paper is as follows: Section 2 presents the mathematical vehicle model under consideration and Section 3 describes the Unscented Kalman Filter implementation. The vehicle tests and the achieved filter performance are discussed in Section 4. Section 5 summarizes the results and gives an outlook on future research activities.

2 Mathematical vehicle modeling

This section presents a vehicle model, which will serve as a basis for the estimator design. The starting point of the modeling is a planar two-track vehicle model with 3 degrees-of-freedom. The roll and the pitch dynamics are consciously omitted in the mathematical formulation in order to reduce the size of the state vector. For calculating the longitudinal and the lateral tire forces, a simplified version of the Magic Formula tire model [26, 27] is used. A new method for the calculation of the vertical tire loads is developed based on quasi-stationary considerations. Finally, all presented sub-models are merged into one model for the estimator design.

2.1 *Planar vehicle model*

A planar two-track vehicle model is presented in this subsection. The following modeling assumptions are made:

- the vehicle is moving on a flat horizontal plane;
- there are neither pitch, nor roll, nor heave dynamical effects;
- the aerodynamic drag force is applied in the road plane, i.e., there is no aerodynamic lift;
- steer angles of the front left and front right wheels are known.[1]

---

[1] The steering wheel angle sensor belongs to the standard VDC system equipment. Therefore, the steer angles of the front wheels can be calculated out of the known steering wheel angle and the kinematics of the steering system. The accuracy can be additionally increased by introducing a detailed steering system model.

Figure 1 shows the vehicle in the inertial reference frame $Oxyz$ and defines the moving body-fixed reference frame $Bxyz$. In this paper, individual wheels are addressed by the subscripts as presented in Table 1.
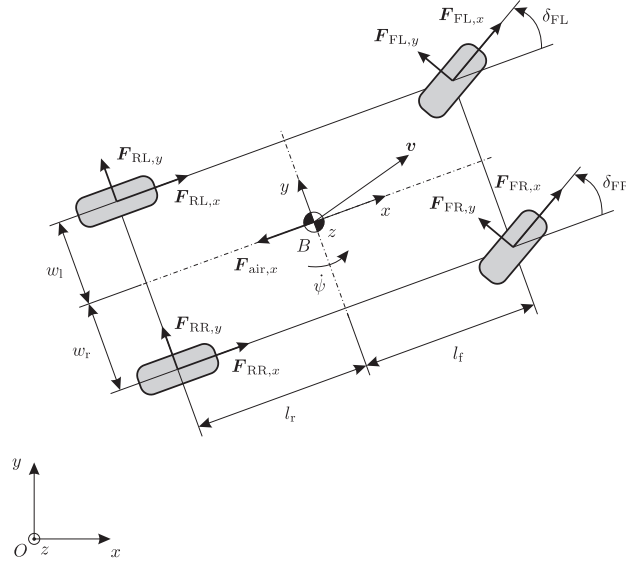

Figure 1. Planar two-track vehicle model: reference frames and acting forces.

Table 1. Abbreviations for the wheel positions

FL	front left	FR	front right
RL	rear left	RR	rear right

Let the vehicle have the total mass m and the moment of inertia I_{zz} about the z-axis. The position of the center of mass (CoM) is defined by the distances to the front axle l_f, to the rear axle l_r, to the left wheels w_l, and to the right wheels w_r. The forces applied to the vehicle are the tire/road contact forces $\boldsymbol{F}_i$, $i \in \{\mathrm{FL}, \mathrm{FR}, \mathrm{RL}, \mathrm{RR}\}$ and the air resistance force $\boldsymbol{F}_\mathrm{air}$. The equations of motion for the vehicle w.r.t. the inertial reference frame $Oxyz$ projected on the body-fixed reference frame $Bxyz$ are given by

$$\frac{\mathrm{d}}{\mathrm{d}t}v_{B,x} = \frac{1}{m}\left(F_{\mathrm{FL},x}\cos\delta_{\mathrm{FL}} + F_{\mathrm{FR},x}\cos\delta_{\mathrm{FR}} - F_{\mathrm{FL},y}\sin\delta_{\mathrm{FL}} - F_{\mathrm{FR},y}\sin\delta_{\mathrm{FR}} + F_{\mathrm{RL},x} + F_{\mathrm{RR},x} - F_{\mathrm{air},x}\right) + \dot{\psi}\,v_{B,y}, \tag{1a}$$

$$\frac{\mathrm{d}}{\mathrm{d}t}v_{B,y} = \frac{1}{m}\left(F_{\mathrm{FL},x}\sin\delta_{\mathrm{FL}} + F_{\mathrm{FR},x}\sin\delta_{\mathrm{FR}} + F_{\mathrm{FL},y}\cos\delta_{\mathrm{FL}} + F_{\mathrm{FR},y}\cos\delta_{\mathrm{FR}} + F_{\mathrm{RL},y} + F_{\mathrm{RR},y}\right) - \dot{\psi}\,v_{B,x}, \tag{1b}$$

$$\frac{\mathrm{d}}{\mathrm{d}t}\dot{\psi} = \frac{1}{I_{zz}}\big((F_{\mathrm{FL},x}\sin\delta_{\mathrm{FL}} + F_{\mathrm{FL},y}\cos\delta_{\mathrm{FL}} + F_{\mathrm{FR},x}\sin\delta_{\mathrm{FR}} + F_{\mathrm{FR},y}\cos\delta_{\mathrm{FR}})\,l_\mathrm{f} - (F_{\mathrm{RL},y} + F_{\mathrm{RR},y})\,l_\mathrm{r} +$$
$$(F_{\mathrm{FR},x}\cos\delta_{\mathrm{FR}} - F_{\mathrm{FR},y}\sin\delta_{\mathrm{FR}} + F_{\mathrm{RR},x})\,w_\mathrm{r} - (F_{\mathrm{FL},x}\cos\delta_{\mathrm{FL}} - F_{\mathrm{FL},y}\sin\delta_{\mathrm{FL}} + F_{\mathrm{RL},x})\,w_\mathrm{l}\big). \tag{1c}$$

The air drag force $F_{\mathrm{air},x}$ is given by the semi-empirical law [25]

$$F_{\mathrm{air},x} = \mathrm{sign}(v_{B,x})\,c_\mathrm{w}\,A\,\frac{\rho}{2}\,v_{B,x}^2, \tag{2}$$

where c_w is the aerodynamic drag coefficient, A the frontal area of the vehicle, ρ the air density, and $v_{B,x}$ the longitudinal vehicle velocity.
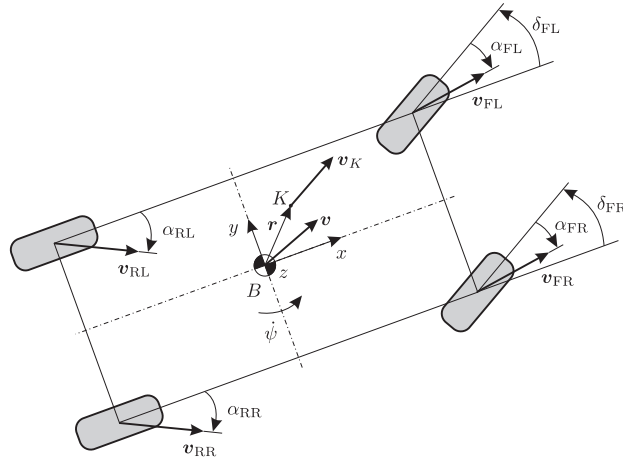
Figure 2. Planar two-track vehicle model: kinematic considerations.

The next step is to define the side-slip angles α_i, $i \in \{\mathrm{FL}, \mathrm{FR}, \mathrm{RL}, \mathrm{RR}\}$ of the individual wheels. For this purpose let us consider a point K whose position w.r.t. the body-fixed reference frame $Bxyz$ is defined by the constant vector $\boldsymbol{r} = [r_x \ r_y \ 0]^T$, see Figure 2. Thus, the velocity of the point K in the body-fixed reference frame $Bxyz$ is given by

$$v_{K,x} = v_{B,x} - \dot{\psi}\, r_y, \quad \text{and} \quad v_{K,y} = v_{B,y} + \dot{\psi}\, r_x. \tag{3}$$

The vehicle is usually operated without spinning about the vertical axis, i.e., the following conditions hold

$$|v_{B,x}| \gg |\dot{\psi}\, r_y| \quad \forall\, |r_y| \leq \max(w_{\mathrm{r}}, w_{\mathrm{l}}). \tag{4}$$

Thus, equations (3) can be simplified to

$$v_{K,x} \approx v_{B,x}, \quad \text{and} \quad v_{K,y} = v_{B,y} + \dot{\psi}\, r_x. \tag{5}$$

With this simplification the side-slip angles can be directly derived from Figure 2 in the following form

$$\alpha_{\mathrm{FL}} = \arctan \frac{v_{\mathrm{FL},y}}{v_{\mathrm{FL},x}} - \delta_{\mathrm{FL}} \approx \frac{v_{B,y} + \dot{\psi}\, l_{\mathrm{f}}}{v_{B,x}} - \delta_{\mathrm{FL}}, \tag{6a}$$

$$\alpha_{\mathrm{FR}} = \arctan \frac{v_{\mathrm{FR},y}}{v_{\mathrm{FR},x}} - \delta_{\mathrm{FR}} \approx \frac{v_{B,y} + \dot{\psi}\, l_{\mathrm{f}}}{v_{B,x}} - \delta_{\mathrm{FR}}, \tag{6b}$$

$$\alpha_{\mathrm{RL}} = \arctan \frac{v_{\mathrm{RL},y}}{v_{\mathrm{RL},x}} \approx \frac{v_{B,y} - \dot{\psi}\, l_{\mathrm{r}}}{v_{B,x}}, \tag{6c}$$

$$\alpha_{\mathrm{RR}} = \arctan \frac{v_{\mathrm{RR},y}}{v_{\mathrm{RR},x}} \approx \frac{v_{B,y} - \dot{\psi}\, l_{\mathrm{r}}}{v_{B,x}}. \tag{6d}$$

Note that the angles in Figure 2 are considered to be positive in the counterclockwise direction. Since the vehicle dynamics strongly depends on the tire properties, the next subsection is devoted to the tire and wheel dynamics modeling.
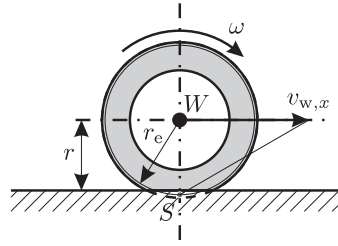
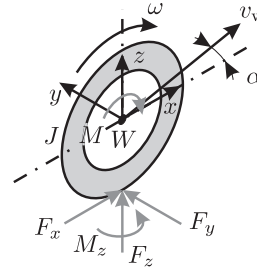Figure 3. Loaded wheel radius r and effective wheel radius r_e.

Figure 4. Wheel forces and torques in the wheel-fixed coordinate system $Wxyz$.

2.2 *Tire model and wheel dynamics*

At first, we will consider the tire force generation and the wheel dynamics for one wheel. Figure 3 shows the free rolling wheel on the flat road. There always exists an instantaneous center of rotation S. The distance between this center of rotation and the wheel axis is called the effective wheel radius r_e. Another important value is the distance between the road plane and the wheel axis, also known as the loaded wheel radius r. The wheel-fixed reference frame $Wxyz$ and applied torques and forces are depicted in Figure 4. The translational velocity of the wheel axis $\boldsymbol{v}_w$ can build a side-slip angle α w.r.t. the wheel center plane Wxz. The rotational velocity of the wheel about the y-axis is denoted by ω. In braking or accelerating situations a longitudinal slip κ occurs

$$\kappa = -\frac{v_{w,x} - \omega\, r_e}{v_{w,x}}, \tag{7}$$

where the longitudinal velocity of the wheel axis (i.e., the projection of $\boldsymbol{v}_w$ on the x-axis of the wheel-fixed reference frame $Wxyz$) is given by $v_{w,x} = \|\boldsymbol{v}_w\| \cos\alpha$, with $\|\cdot\|$ denoting the Euclidian norm. The lateral side-slip angle α and the longitudinal slip κ cause the lateral F_y and longitudinal F_x tire forces, as well as the aligning torque M_z. These forces and the torque depend on the given tire properties and the actual environmental conditions. In this contribution, the main physical effects are reproduced by using Magic Formula [26, 27], which is a reliable phenomenological tire model for vehicle dynamics simulation and analysis. For the sake of simplicity, we will neglect the aligning torque M_z, the nonlinear influence of the vertical tire force F_z, and the minor effects due to wheel camber, conicity and ply steer.

At first, the longitudinal and the lateral tire forces F_{x0} and F_{y0} are calculated under the assumption that there are only decoupled slip conditions. The coupling of the longitudinal and the lateral tire forces by combined slip conditions is taken into account in a second step by means of the weighting functions $G_{x\alpha}$ and $G_{y\kappa}$. The combined slip tire forces F_x and F_y are given by [26]

$$F_x = G_{x\alpha}\, F_{x0} \quad \text{and} \quad F_y = G_{y\kappa}\, F_{y0}. \tag{8}$$

The nominal longitudinal tire/road contact force F_{x0} is calculated by

$$F_{x0} = F_z\, \mu_{max} \sin\Big(C_x \arctan\big(B_x\,\kappa - E_x\,(B_x\,\kappa - \arctan(B_x\,\kappa))\big)\Big). \tag{9}$$

Here and in the following, $C_i, B_i, E_i,\ i \in \{x, y, x\alpha, y\kappa\}$ denote tire model parameters.[1] The variable μ_{max} defines the tire/road grip conditions. The nominal lateral tire/road contact force F_{y0} reads as

$$F_{y0} = F_z\, \mu_{max} \sin\Big(C_y \arctan\big(B_y\,\alpha - E_y\,(B_y\,\alpha - \arctan(B_y\,\alpha))\big)\Big). \tag{10}$$

---

[1]These parameters are also referred to as Magic Formula tire parameters and are only valid for a given velocity, tire, and road surface. Practically they are extracted from tire measurement data by means of an optimization procedure.

The combined slip conditions are considered in (8) by means of the weighting functions $G_{x\alpha}$ and $G_{y\kappa}$. These empiric bell-shaped cosine functions depend on the complementary slip conditions. A simplified approach is used for the longitudinal force weighting function $G_{x\alpha}$

$$G_{x\alpha} = \cos \Big(C_{x\alpha} \arctan(B_{x\alpha}\alpha - E_{x\alpha}(B_{x\alpha}\alpha - \arctan\alpha)) \Big). \tag{11}$$

The parameters $B_{x\alpha}$ and $E_{x\alpha}$ define the shape of $G_{x\alpha}$, and the parameter $C_{x\alpha}$ determines the characteristics of $G_{x\alpha}$ for high slip angles. For the calculation of $G_{y\kappa}$, an additional physical effect is taken into account. There is a small increase in the lateral force during braking and a small decrease during acceleration. This asymmetry of the lateral forces is considered by means of a horizontal shift $S_{Hy\kappa}$ of the weighting function $G_{y\kappa}$. The weighting function $G_{y\kappa}$ is given by

$$G_{y\kappa} = \frac{\cos\left(C_{y\kappa}\arctan\left(B_{y\kappa}\left(\kappa + S_{Hy\kappa}\right)\right)\right)}{\cos\left(C_{y\kappa}\arctan\left(B_{y\kappa}S_{Hy\kappa}\right)\right)}. \tag{12}$$

Typical tire characteristics due to equations (8)-(12) are depicted in Figure 5.
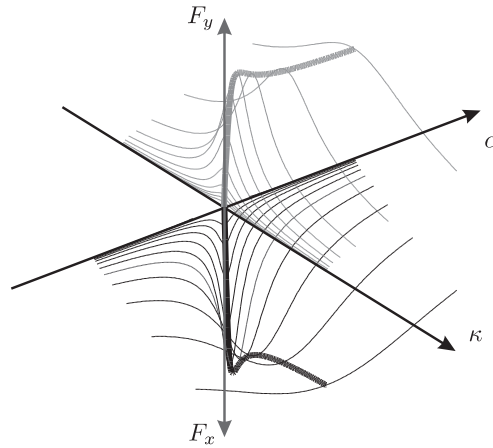

Figure 5. Typical tire characteristics calculated by means of the simplified Magic Formula equations (8)-(12).

At this point, the longitudinal and the lateral tire forces are specified by means of the tire model. Let us recall Figure 4 to derive the mathematical model for the wheel dynamics. In general, there are braking and propulsion torques, M_{b} and M_{p}, acting on the wheel. They produce a total torque $M = M_{\mathrm{p}} - M_{\mathrm{b}}$ which counteracts the torque due to the longitudinal wheel force F_x. Thus, the principle of conservation of angular wheel momentum about the x-axis yields

$$\frac{\mathrm{d}}{\mathrm{d}t}\omega = \frac{1}{J}\left(M - F_x r\right), \tag{13}$$

where J denotes the rotational mass moment of inertia of the wheel.

Since the vertical tire force F_z is essential for the calculation of the lateral and of the longitudinal tire forces (cf. equations (9) and (10)), a strategy for the determination of the vertical tire forces will be developed in the next subsection.

2.3   Calculation of vertical tire forces

The following calculation of the vertical tire forces is based on quasi-stationary considerations. The underlying vehicle model is depicted in Figure 6. Thereby, it is assumed that the vehicle is on an horizontal even surface. The vehicle body is assumed to be rigid for the sake of simplicity. Tires, wheel suspensions,
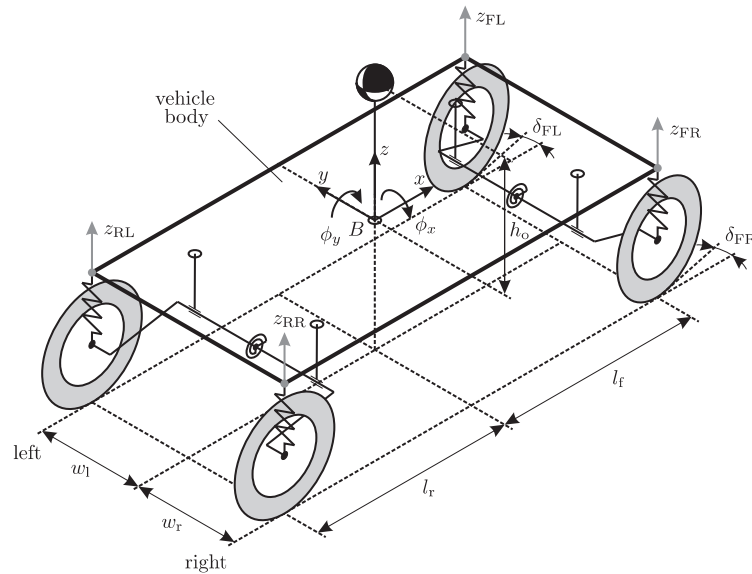
Figure 6. Vehicle model for calculation of the vertical tire forces.

and stabilizers are treated as massless linear springs. Moreover, let us assume that the front and the rear axle are solely coupled via the rigid vehicle body. All considerations will be performed w.r.t. the vehicle body-fixed reference frame $Bxyz$. The position of the center of mass is expressed in terms of the distances to the front and rear axle, l_f and l_r, the distance to the origin of the body-fixed reference frame $Bxyz$ denoted by h_o, and the distances to the left and to the right wheels, w_l and w_r, respectively (cf. Figure 6). The calculation method for the vertical tire forces is based on the following considerations:

- the forces applied to the vehicle's center of mass are treated as model inputs;
- the displacement of the vehicle body is calculated out of the torque and force equilibrium conditions using known stiffnesses and the geometric properties;
- once the position of the vehicle body is known, the vertical tire forces are computed by means of the spring force characteristics.

It is assumed that, if there are no forces applied to the vehicle's center of mass, then the vehicle body is horizontally aligned. The displacement from this reference position $\boldsymbol{\xi}_\mathrm{o} = [0\ 0\ 0]^T$ can be described by rotations ϕ_x and ϕ_y about the x- and the y-axis, and by a translation d_z in z-direction, i.e., $\boldsymbol{\xi} = [\phi_x\ \phi_y\ d_z]^T$. For all further derivations, the rotations of the vehicle body, ϕ_x and ϕ_y, are assumed to be small, i.e.,

$$\sin\phi_i \approx \phi_i, \quad \cos\phi_i \approx 1, \quad i \in \{x, y\}. \tag{14}$$

The movement of the vehicle body shifts an arbitrary point $\boldsymbol{p} = [x_\mathrm{p}\ y_\mathrm{p}\ 0]^T$ to a point $\boldsymbol{p}^* = [x_\mathrm{p}^*\ y_\mathrm{p}^*\ z_\mathrm{p}^*]^T$, given by the following relation

$$\boldsymbol{p}^* = \begin{bmatrix} 1 & 0 & \phi_y \\ 0 & 1 & -\phi_x \\ -\phi_y & \phi_x & 1 \end{bmatrix} \boldsymbol{p} + \begin{bmatrix} 0 \\ 0 \\ d_z \end{bmatrix}. \tag{15}$$

Consequently, the vertical displacement z_p^* reads as

$$z_\mathrm{p}^* = -\phi_y x_\mathrm{p} + \phi_x y_\mathrm{p} + d_z. \tag{16}$$

According to equation (16), the relative displacements of the suspension mounting points are obtained by

$$
\underbrace{\begin{bmatrix} z_{\mathrm{FL}} \\ z_{\mathrm{FR}} \\ z_{\mathrm{RL}} \\ z_{\mathrm{RR}} \end{bmatrix}}_{\boldsymbol{z}} = \underbrace{\begin{bmatrix} w_{\mathrm{l}} & -l_{\mathrm{f}} & 1 \\ -w_{\mathrm{r}} & -l_{\mathrm{f}} & 1 \\ w_{\mathrm{l}} & l_{\mathrm{r}} & 1 \\ -w_{\mathrm{r}} & l_{\mathrm{r}} & 1 \end{bmatrix}}_{\boldsymbol{T}_{\mathrm{A}}} \underbrace{\begin{bmatrix} \phi_x \\ \phi_y \\ d_z \end{bmatrix}}_{\boldsymbol{\xi}} . \tag{17}
$$

The vehicle body displacement causes changes in the vertical suspension and the tire forces. Recall that the interaction of the front and the rear suspension was assumed to take place only via the rigid vehicle body. Therefore, if the vehicle body position is known, it suffices to investigate the front and the rear axle independently. In Figure 7 one axle is shown for the case of the displaced vehicle body.
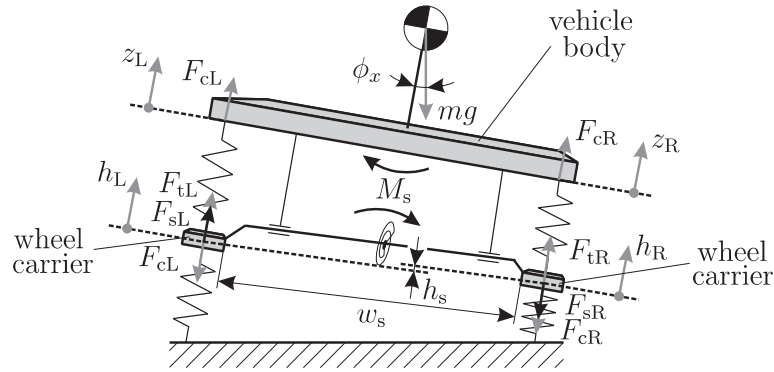

Figure 7. One axle of the vehicle: suspensions, tires, and stabilizer are represented as springs.

As already mentioned, the wheel suspensions, the stabilizer and the tires are considered to be linear springs. Let us denote the corresponding stiffnesses by c_c, c_s, and c_t. For the sake of simplicity, the stiffnesses of the left and the right side are assumed to be equal. The distance between the two wheel carriers is denoted by w_{s} (cf. Figure 7). The displacements of the suspension mounting points z_{L} and z_{R} as well as of the wheel carriers h_{L} and h_{R} are defined w.r.t. the reference position, in which the vehicle body is horizontal and no forces are acting on the vehicle's center of mass. The vertical tire forces F_{tL} and F_{tR} are given by (considering the horizontal even road surface)

$$
F_{\mathrm{tL}} = -c_t h_{\mathrm{L}} \quad \text{and} \quad F_{\mathrm{tR}} = -c_t h_{\mathrm{R}}. \tag{18}
$$

The suspension forces F_{cL} and F_{cR} yield

$$
F_{\mathrm{cL}} = c_c(h_{\mathrm{L}} - z_{\mathrm{L}}) \quad \text{and} \quad F_{\mathrm{cR}} = c_c(h_{\mathrm{R}} - z_{\mathrm{R}}). \tag{19}
$$

If the vehicle rolls, the stabilizer causes the reaction forces F_{sL} and F_{sR} on the wheel carriers and on the chassis. This effect is modeled by a linear spring with the stiffness c_s acting between the two wheel carriers. In this case, the stabilizer forces F_{sL} and F_{sR} are proportional to the relative displacement $h_{\mathrm{s}} = (z_{\mathrm{L}} - h_{\mathrm{L}}) - (z_{\mathrm{R}} - h_{\mathrm{R}})$ of the wheel carriers (see Figure 7). The stabilizer force $|F_{\mathrm{s}}| = |F_{\mathrm{sL}}| = |F_{\mathrm{sR}}|$ becomes

$$
F_{\mathrm{s}} = c_s h_{\mathrm{s}} = c_s \left(z_{\mathrm{L}} - h_{\mathrm{L}} - z_{\mathrm{R}} + h_{\mathrm{R}} \right). \tag{20}
$$

The pair of forces F_{sL} and F_{sR} induces a torque M_{s} acting on the stabilizer bar. There is also the reaction torque of the same magnitude M_{s} that acts on the vehicle body about the x-axis and reduces the roll angle. The corresponding absolute value is given by

$$
M_{\mathrm{s}} = -w_{\mathrm{s}} F_{\mathrm{s}} = -w_{\mathrm{s}} c_s \left(z_{\mathrm{L}} - h_{\mathrm{L}} - z_{\mathrm{R}} + h_{\mathrm{R}} \right). \tag{21}
$$

The static force equilibrium of the wheel carriers results in the two equations

$$-F_{cL} + F_{sL} + F_{tL} = 0 \quad \text{and} \quad -F_{cR} - F_{sR} + F_{tR} = 0. \tag{22}$$

By inserting the force laws (18), (19) into (22), we get

$$\underbrace{\begin{bmatrix} c_c + c_t + c_s & -c_s \\ -c_s & c_c + c_t + c_s \end{bmatrix}}_{\boldsymbol{T}_U} \begin{bmatrix} h_L \\ h_R \end{bmatrix} = \underbrace{\begin{bmatrix} c_c + c_s & -c_s \\ -c_s & c_c + c_s \end{bmatrix}}_{\boldsymbol{T}_E} \begin{bmatrix} z_L \\ z_R \end{bmatrix}. \tag{23}$$

These relations written for the front and the rear axle result in

$$\boldsymbol{T}_{U_F} \begin{bmatrix} h_{FL} \\ h_{FR} \end{bmatrix} = \boldsymbol{T}_{E_F} \begin{bmatrix} z_{FL} \\ z_{FR} \end{bmatrix} \quad \text{and} \quad \boldsymbol{T}_{U_R} \begin{bmatrix} h_{RL} \\ h_{RR} \end{bmatrix} = \boldsymbol{T}_{E_R} \begin{bmatrix} z_{RL} \\ z_{RR} \end{bmatrix}. \tag{24}$$

Here and subsequently, the subscripts F and R always refer to the front and the rear axle, respectively. Considering equation (21), we obtain the stabilizer torques at the front and at the rear axle in the form

$$M_{sF} = -w_{sF} c_{sF} \left(z_{FL} - h_{FL} - z_{FR} + h_{FR} \right), \tag{25a}$$

$$M_{sR} = -w_{sR} c_{sR} \left(z_{RL} - h_{RL} - z_{RR} + h_{RR} \right). \tag{25b}$$

Solving the equations (24) for the displacements[1] h_i, $i \in \{FL, FR, RL, RR\}$ and merging the results yields

$$\underbrace{\begin{bmatrix} h_{FL} \\ h_{FR} \\ h_{RL} \\ h_{RR} \end{bmatrix}}_{\boldsymbol{h}} = \begin{bmatrix} \boldsymbol{T}_{U_F}^{-1} \boldsymbol{T}_{E_F} & \boldsymbol{0} \\ \boldsymbol{0} & \boldsymbol{T}_{U_R}^{-1} \boldsymbol{T}_{E_R} \end{bmatrix} \underbrace{\begin{bmatrix} z_{FL} \\ z_{FR} \\ z_{RL} \\ z_{RR} \end{bmatrix}}_{\boldsymbol{z}}. \tag{26}$$

Figure 8 depicts all relevant forces and torques acting on the vehicle. The inertial forces F_x and F_y act on the center of mass, since we are working in the vehicle-fixed reference frame. The forces generated at the contact patches are denoted by $F_{k,j}$, where $k \in \{FL, FR, RL, RR\}$ and $j \in \{x, y\}$. The braking and propulsion torques applied to the individual wheels are addressed by $M_i = M_{p,i} - M_{b,i}$, where $i \in \{FL, FR, RL, RR\}$.

The displacement of the vehicle body is determined by the suspension forces F_{ci}, where $i \in \{FL, FR, RL, RR\}$, and the stabilizer torques M_{sF} and M_{sR}. With the help of equations (19) and (26) the suspension force vector $\boldsymbol{f}_c$ takes the form

$$\boldsymbol{f}_c = \begin{bmatrix} F_{cFL} \\ F_{cFR} \\ F_{cRL} \\ F_{cRR} \end{bmatrix} = \underbrace{\begin{bmatrix} c_{c_F} (\boldsymbol{T}_{U_F}^{-1} \boldsymbol{T}_{E_F} - \boldsymbol{I}) & \boldsymbol{0} \\ \boldsymbol{0} & c_{c_R} (\boldsymbol{T}_{U_R}^{-1} \boldsymbol{T}_{E_R} - \boldsymbol{I}) \end{bmatrix}}_{\boldsymbol{T}_C} \boldsymbol{z}, \tag{27}$$

---

[1]Note that the matrix $\boldsymbol{T}_U$ is invertible as long as c_t or c_c are unequal to zero.
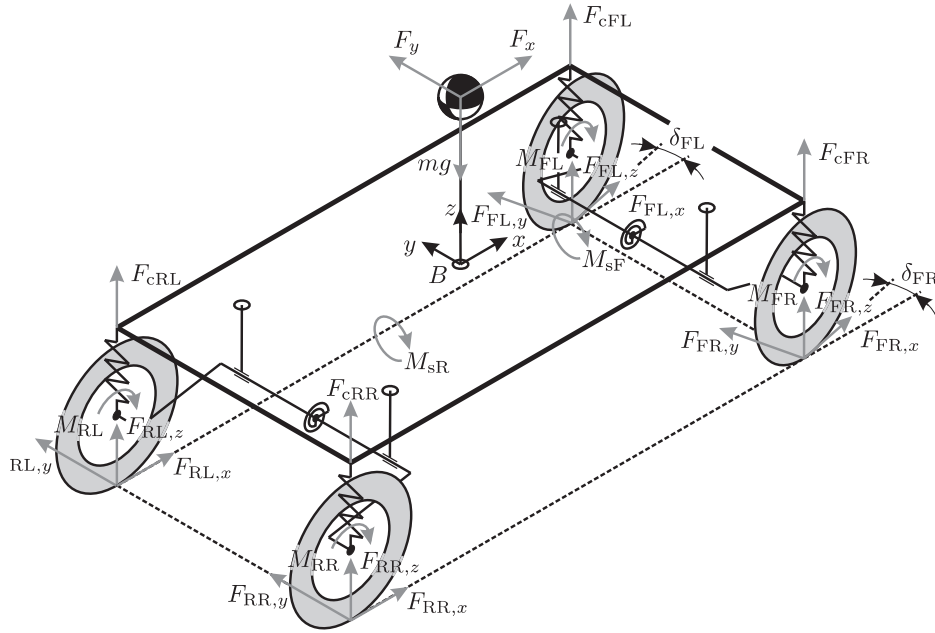
Figure 8. Forces and torques relevant for the vertical tire forces calculation.

where c_{c_F} and c_{c_R} are the suspension stiffnesses of the front and the rear axle, respectively. In a similar manner, by considering (18) and (26), the vertical tire force vector $\boldsymbol{f}_t$ yields

$$\boldsymbol{f}_t = \begin{bmatrix} F_{FL,z} \\ F_{FR,z} \\ F_{RL,z} \\ F_{RR,z} \end{bmatrix} = \begin{bmatrix} F_{tFL} \\ F_{tFR} \\ F_{tRL} \\ F_{tRR} \end{bmatrix} = \underbrace{\begin{bmatrix} -c_{t_F}\boldsymbol{T}_{U_F}^{-1}\boldsymbol{T}_{E_F} & \boldsymbol{0} \\ \boldsymbol{0} & -c_{t_R}\boldsymbol{T}_{U_R}^{-1}\boldsymbol{T}_{E_R} \end{bmatrix}}_{\boldsymbol{T}_P}\boldsymbol{z}, \tag{28}$$

where c_{t_F} and c_{t_R} are the tire stiffnesses of the front and the rear axle.
From (25) the total torque M_{sC} generated by the stabilizers is given by

$$M_{sC} = M_{sF} + M_{sR} = \begin{bmatrix} -w_{sF}c_{sF}, & w_{sF}c_{sF}, & -w_{sR}c_{sR}, & w_{sR}c_{sR} \end{bmatrix}(\boldsymbol{z} - \boldsymbol{h}). \tag{29}$$

Substituting (26) into (29) results in

$$M_{sC} = \underbrace{\begin{bmatrix} -w_{sF}c_{sF}, & w_{sF}c_{sF}, & -w_{sR}c_{sR}, & w_{sR}c_{sR} \end{bmatrix}\left(\boldsymbol{I} - \begin{bmatrix} \boldsymbol{T}_{U_F}^{-1}\boldsymbol{T}_{E_F} & \boldsymbol{0} \\ \boldsymbol{0} & \boldsymbol{T}_{U_R}^{-1}\boldsymbol{T}_{E_R} \end{bmatrix}\right)}_{\boldsymbol{t}_S^T}\boldsymbol{z}. \tag{30}$$

As already mentioned before, a quasi-stationary vehicle motion is assumed for the calculation of the vertical tire forces. Therefore, we consider the static equilibrium of the vehicle body (cf. Figure 8). The torque balance equations about the y- and the x-axis and the force equilibrium along the z-axis are given by

$$-(F_{cFL} + F_{cFR})\,l_f + (F_{cRL} + F_{cRR})\,l_r + F_x h_o \cos\phi_y + mgh_o \sin\phi_y = 0 \tag{31a}$$

$$(F_{cFL} + F_{cRL})\,w_l - (F_{cFR} + F_{cRR})\,w_r - F_y h_o \cos\phi_x + mgh_o \sin\phi_x + M_{sC} = 0 \tag{31b}$$

$$(F_{cFL} + F_{cFR} + F_{cRL} + F_{cRR})\cos\phi_y - mg = 0. \tag{31c}$$

Using the fact that the angles ϕ_x and ϕ_y are small and considering equation (30), we can express (31) in vector form

$$\underbrace{\begin{bmatrix} w_{\mathrm{l}} & -w_{\mathrm{r}} & w_{\mathrm{l}} & -w_{\mathrm{r}} \\ -l_{\mathrm{f}} & -l_{\mathrm{f}} & l_{\mathrm{r}} & l_{\mathrm{r}} \\ 1 & 1 & 1 & 1 \end{bmatrix}}_{\boldsymbol{T}_{\mathrm{A}}^{T}} \underbrace{\begin{bmatrix} F_{\mathrm{cFL}} \\ F_{\mathrm{cFR}} \\ F_{\mathrm{cRL}} \\ F_{\mathrm{cRR}} \end{bmatrix}}_{\boldsymbol{f}_{\mathrm{c}}} = \underbrace{\begin{bmatrix} F_y\,h_{\mathrm{o}} \\ -F_x\,h_{\mathrm{o}} \\ mg \end{bmatrix}}_{\boldsymbol{f}_{\mathrm{in}}} + \begin{bmatrix} -mgh_{\mathrm{o}} & 0 & 0 \\ 0 & -mgh_{\mathrm{o}} & 0 \\ 0 & 0 & 0 \end{bmatrix} \underbrace{\begin{bmatrix} \phi_x \\ \phi_y \\ d_z \end{bmatrix}}_{\boldsymbol{\xi}} - \begin{bmatrix} \boldsymbol{t}_{\mathrm{s}}^{T} \\ \boldsymbol{0}^{T} \\ \boldsymbol{0}^{T} \end{bmatrix} \boldsymbol{z}. \tag{32}$$

Subsequent substitution of equations (27) and (17) into (32) yields

$$\boldsymbol{T}_{\mathrm{A}}^{T}\boldsymbol{T}_{\mathrm{C}}\boldsymbol{T}_{\mathrm{A}}\,\boldsymbol{\xi} = \boldsymbol{f}_{\mathrm{in}} + \underbrace{\left(\begin{bmatrix} -mgh_{\mathrm{o}} & 0 & 0 \\ 0 & -mgh_{\mathrm{o}} & 0 \\ 0 & 0 & 0 \end{bmatrix} - \begin{bmatrix} \boldsymbol{t}_{\mathrm{s}}^{T} \\ \boldsymbol{0}^{T} \\ \boldsymbol{0}^{T} \end{bmatrix} \boldsymbol{T}_{\mathrm{A}} \right)}_{\boldsymbol{T}_{\mathrm{K}}} \boldsymbol{\xi}. \tag{33}$$

Solving equation (33) for the vehicle body displacement $\boldsymbol{\xi} = [\phi_x\ \phi_y\ d_z]^{T}$ results in[1]

$$\boldsymbol{\xi} = (\boldsymbol{T}_{\mathrm{A}}^{T}\boldsymbol{T}_{\mathrm{C}}\boldsymbol{T}_{\mathrm{A}} - \boldsymbol{T}_{\mathrm{K}})^{-1}\,\boldsymbol{f}_{\mathrm{in}}, \tag{34}$$

Thus, the vertical tire forces $\boldsymbol{f}_{\mathrm{t}}$ can be calculated by substitution of equations (34) and (17) into (28) in the form

$$\underbrace{\begin{bmatrix} F_{\mathrm{FL},z} \\ F_{\mathrm{FR},z} \\ F_{\mathrm{RL},z} \\ F_{\mathrm{RR},z} \end{bmatrix}}_{\boldsymbol{f}_{\mathrm{t}}} = \underbrace{\boldsymbol{T}_{\mathrm{P}}\boldsymbol{T}_{\mathrm{A}}(\boldsymbol{T}_{\mathrm{A}}^{T}\boldsymbol{T}_{\mathrm{C}}\boldsymbol{T}_{\mathrm{A}} - \boldsymbol{T}_{\mathrm{K}})^{-1}}_{\boldsymbol{T}_{\mathrm{M}}} \underbrace{\begin{bmatrix} F_y\,h_{\mathrm{o}} \\ -F_x\,h_{\mathrm{o}} \\ mg \end{bmatrix}}_{\boldsymbol{f}_{\mathrm{in}}}. \tag{35}$$

It is worth mentioning that the matrix $\boldsymbol{T}_{\mathrm{M}}$ in equation (35) is time-invariant and can therefore be calculated for each vehicle in advance. The proposed method has a clear physical interpretation and – in contrast to the methods known from the literature, for example [25] – it additionally considers the stiffnesses of the tires. This allows us to increase the accuracy of the vertical tire forces calculation. For example, calculating (35) with parameters of a passenger vehicle and a typical vertical tire stiffness of about $0,2{\cdot}10^{6}$ N/m yields about 5% higher vertical tire forces in comparison to the case with rigid tires. However, if the suspension stiffnesses are considered to be equal in the front and in the rear, and the tire stiffnesses are supposed to be infinitely large, then the obtained results are equal to the results given in [25].

2.4 *Complete vehicle model*

In this subsection, all presented sub-models are merged together into a complete vehicle model. An algebraic loop, which is caused by the vertical tire forces calculation, is explicitly eliminated in order to achieve a continuous state space representation. Finally, the discretization of this nonlinear model for the estimator design is discussed.

Eliminating algebraic loop. The inertial forces F_x and F_y are required for determining the vertical tire forces according to (35). The considered inertial forces

$$F_x = -m\,a_{B,x} = -m(\dot{v}_{B,x} - \dot{\psi}\,v_{B,y}) \quad \text{and} \quad F_y = -m\,a_{B,y} = -m(\dot{v}_{B,y} + \dot{\psi}\,v_{B,x}) \tag{36}$$

---

[1]Note that the matrix $(\boldsymbol{T}_{\mathrm{A}}^{T}\boldsymbol{T}_{\mathrm{C}}\boldsymbol{T}_{\mathrm{A}} - \boldsymbol{T}_{\mathrm{K}})$ is always invertible for physically consistent vehicle parameters

can be calculated out of the two-track model (1a), (1b) as well as the tire models (6)–(12). Unfortunately, the longitudinal and lateral tire forces depend on the vertical tire forces. This algebraic loop will be eliminated before the state space description of the complete vehicle model is introduced. Considering the two-track model (1a), (1b) together with the individual tire forces (6)-(12) and equation (36) for the inertial tire forces, we can express $\boldsymbol{f}_{\text{in}}$ in the form

$$\boldsymbol{f}_{\text{in}} = \begin{bmatrix} F_y\, h_{\text{o}} \\ -F_x\, h_{\text{o}} \\ mg \end{bmatrix} = \underbrace{\begin{bmatrix} a_{11} & a_{12} & a_{13} & a_{14} \\ a_{21} & a_{22} & a_{23} & a_{24} \\ 0 & 0 & 0 & 0 \end{bmatrix}}_{\boldsymbol{T}_{\text{sys1}}(\cdot)} \begin{bmatrix} F_{\text{FL},z} \\ F_{\text{FR},z} \\ F_{\text{RL},z} \\ F_{\text{RR},z} \end{bmatrix} + \underbrace{\begin{bmatrix} 0 \\ F_{air,x} \\ mg \end{bmatrix}}_{\boldsymbol{t}_{\text{sys2}}(\cdot)}. \tag{37}$$

The elements of the matrix $\boldsymbol{T}_{\text{sys1}}(\cdot)$ and of the vector $\boldsymbol{t}_{\text{sys2}}(\cdot)$ not only depend on the vehicle parameters but also on the vehicle state variables $v_{B,x}, v_{B,y}, \dot{\psi}, \omega_k, k \in \{\text{FL}, \text{FR}, \text{RL}, \text{RR}\}$, and on the steer angles $\delta_{\text{FL}}, \delta_{\text{FR}}$. Substituting (37) into (35) and solving for the vertical tire forces $\boldsymbol{f}_{\text{t}}$ yields

$$\underbrace{\begin{bmatrix} F_{\text{FL},z} \\ F_{\text{FR},z} \\ F_{\text{RL},z} \\ F_{\text{RR},z} \end{bmatrix}}_{\boldsymbol{f}_{\text{t}}} = \left(\boldsymbol{I} - \boldsymbol{T}_{\text{M}}\, \boldsymbol{T}_{\text{sys1}}(\cdot) \right)^{-1} \boldsymbol{T}_{\text{M}}\, \boldsymbol{t}_{\text{sys2}}(\cdot). \tag{38}$$

The presented model has the beneficial property that the vertical tire forces can be explicitly calculated, if the vehicle steer angles $\delta_{\text{FL}}, \delta_{\text{FR}}$ and the vehicle states are known. This allows us to formulate an explicit state space formulation of the complete vehicle model.

Continuous state space form. Figure 2.4 shows a block diagram of the complete vehicle model for estimator design consisting of

- the tire force calculation and the wheel dynamics for each of the four wheels (6)–(13),
- the planar vehicle body dynamics (1),
- the vertical tire forces calculation (38), and
- the road grip coefficient μ_{max}

Since the focus of this work lies on the correct state estimation under changing grip conditions, we assume the road grip factor μ_{max} to be an unknown but constant parameter that is identical for all tires. Thus, an exogenous model of the form $\dot{\mu}_{\text{max}}(t) = 0$ is added to the system's equations which serve as a basis for the Kalman filter design. At this point it is worth noting that it is not expected that the estimated value of μ_{max} will give an exact average value of the actual grip conditions. It rather provides an additional degree-of-freedom for the estimator to minimize the underlying objective functional and thus to adjust the mathematical model with given model structure to the actual measurements. In this sense, the quantitative values of the estimated μ_{max} need not be physically meaningful.

In summary, the complete vehicle model in the continuous state space form reads as

$$\dot{\boldsymbol{x}}(t) = \tilde{\boldsymbol{f}}\Big(\boldsymbol{x}(t), \boldsymbol{u}(t) \Big), \tag{39a}$$

$$\boldsymbol{y}(t) = \tilde{\boldsymbol{h}}\Big(\boldsymbol{x}(t), \boldsymbol{u}(t) \Big), \tag{39b}$$

Figure 9. Block diagram of the complete vehicle model, where $i \in \{\text{FL}, \text{FR}, \text{RL}, \text{RR}\}$ refers to different wheels.

with the input, state, and measurement vectors given by

$$
\boldsymbol{u}(t) = \begin{bmatrix} \delta_{FL}(t) \\ \delta_{FR}(t) \\ M_{p,FL}(t) \\ M_{p,FR}(t) \\ M_{p,RL}(t) \\ M_{p,RR}(t) \\ M_{b,FL}(t) \\ M_{b,FR}(t) \\ M_{b,RL}(t) \\ M_{b,RR}(t) \end{bmatrix}, \quad
\boldsymbol{x}(t) = \begin{bmatrix} v_{B,x}(t) \\ v_{B,y}(t) \\ \dot{\psi}(t) \\ \omega_{FL}(t) \\ \omega_{FR}(t) \\ \omega_{RL}(t) \\ \omega_{RR}(t) \\ \mu_{\max}(t) \end{bmatrix}, \quad
\boldsymbol{y}(t) = \begin{bmatrix} a_{B,y}(t) \\ \dot{\psi}(t) \\ \omega_{FL}(t) \\ \omega_{FR}(t) \\ \omega_{RL}(t) \\ \omega_{RR}(t) \end{bmatrix}.
\tag{40}
$$

Discrete state space form. To get the discrete form representation of the system (39), the zero-order-hold assumption for the system input vector $\boldsymbol{u}(t)$ during the sampling time T_0 is used. This allows us to apply the Taylor-Lie series discretization approach (for more details the reader is referred to [28]) in the form

$$
x_i(k+1) = x_i(k) + \sum_{l=1}^{N_i} \left(L_{\tilde{\boldsymbol{f}}}^l \, x_i \right)\Big|_{\boldsymbol{x}(k), \boldsymbol{u}(k)} \frac{T_0^l}{l\,!}.
\tag{41}
$$

Thereby, k refers to the discrete time step, $i = 1, \ldots, 8$ denotes the ith element of the state vector $\boldsymbol{x}$, N_i is the truncation order of the Taylor-Lie series, and $L_{\tilde{\boldsymbol{f}}}^l x_i$ is the lth order Lie derivative of x_i along the vector field[1] $\tilde{\boldsymbol{f}}$. In order to reduce the computational effort, the Taylor-Lie series of order $N = 1$ is used for the states $v_{B,x}, v_{B,y}, \dot{\psi}$, and $\mu_{\max}$. This choice corresponds to the classical forward Euler integration. Due to the faster wheel dynamics, the order $N = 2$ is chosen for the states ω_k, $k \in \{\text{FL}, \text{FR}, \text{RL}, \text{RR}\}$ in order to improve the calculation accuracy. Introducing the stochastic process noise $\boldsymbol{\omega}$ and the stochastic

---

[1] Note that within one sampling interval T_0 equation (39a) is an autonomous system, since $\boldsymbol{u}(k)$ is constant due to the zero-order-hold assumption.

measurement noise $\boldsymbol{\nu}$, we obtain the final system description for the filter design in the form

$$\boldsymbol{x}(k+1) = \boldsymbol{f}\Big(\boldsymbol{x}(k), \boldsymbol{u}(k)\Big) + \boldsymbol{\omega}(k), \tag{42}$$

$$\boldsymbol{y}(k) = \boldsymbol{h}\Big(\boldsymbol{x}(k), \boldsymbol{u}(k)\Big) + \boldsymbol{\nu}(k). \tag{43}$$

3   Estimator design for vehicle states

The well known Kalman filter [29] uses a Gaussian approximation of the random state, measurement, and noise variables. This allows us to completely describe the stochastic variables just by their mean values and covariances. If we consider a linear dynamical system, then transformations of the Gaussian random variables through the dynamic and the measurement equations will always result in Gaussian random variables. This feature enables the calculation of the feedback Kalman gain out of the prior state estimation and the posterior innovation. The well known solution for nonlinear systems state estimation is the Extended Kalman Filter (EKF), which uses the linearization of the nonlinear system by means of a first order Taylor series expansion around the latest estimate (cf. [30]). This approach enforces the calculation of the system Jacobian matrix at every estimation step and induces linearization errors. Thus, this procedure entails biasing of the prediction errors and a distortion of the propagated covariance information. A popular way to keep these errors bounded is the reduction of the sampling time.

Another application of Kalman ideas to the state estimation of nonlinear systems is the Unscented Kalman Filter (UKF), discussed in [23,24]. The UKF also approximates the statistic properties of the random variables up to the second order. In contrast to EKF, not the mean value and covariance but a minimal set of carefully chosen weighted sample points, the so-called sigma points, are used for the approximation. These points are explicitly propagated through the nonlinear system equations and yield some nonlinear stochastic description of the random variables. These variables are approximated afterwards by Gaussian random variables, what enables the usage of the standard equations for the Kalman gain calculation. In this way, the UKF achieves higher accuracy in comparison to the EKF by requiring comparable computational effort [24]. In the following, some essential UKF results after [23,24] are reformulated yielding a numerical efficient esimator algotithm.

Let us consider the nonlinear time-discrete dynamical system (42), (43) with state $\boldsymbol{x} \in \mathbb{R}^n$, input $\boldsymbol{u} \in \mathbb{R}^p$, measurement output $\boldsymbol{y} \in \mathbb{R}^m$, process noise $\boldsymbol{w} \in \mathbb{R}^n$ and measurement noise $\boldsymbol{\nu} \in \mathbb{R}^m$. The random variables $\boldsymbol{w}$ and $\boldsymbol{\nu}$ are assumed to be white Gaussian uncorrelated noises having the following properties

$$E[\boldsymbol{w}(k)] = \boldsymbol{0} \quad \text{and} \quad E[\boldsymbol{w}(k)\,\boldsymbol{w}(l)^T] = \boldsymbol{Q}\,\delta_{kl}, \qquad \forall k, l \geq 0, \tag{44}$$

$$E[\boldsymbol{\nu}(k)] = \boldsymbol{0} \quad \text{and} \quad E[\boldsymbol{v}(k)\,\boldsymbol{v}(l)^T] = \boldsymbol{R}\,\delta_{kl}, \qquad \forall\, k, l \geq 0, \tag{45}$$

$$E[\boldsymbol{w}(k)\,\boldsymbol{v}(l)^T] = \boldsymbol{0}, \qquad\qquad\qquad \forall\, k, l \geq 0, \tag{46}$$

where $\boldsymbol{Q} \in \mathbb{R}^{n \times n}$ and $\boldsymbol{R} \in \mathbb{R}^{m \times m}$ are positive definite matrices and δ_{kl} is the Kronecker delta, i.e., $\delta_{kl} = 1$ for $k = l$ and $\delta_{kl} = 0$ otherwise. The initial mean value of $\boldsymbol{x}$ and the initial covariance matrix $\boldsymbol{P}_x$ of the estimation error $\boldsymbol{e} = \boldsymbol{x} - \hat{\boldsymbol{x}}$ are given by

$$\hat{\boldsymbol{x}}_0 = E[\boldsymbol{x}_0] \quad \text{and} \quad \boldsymbol{P}_{x_0} = E[(\boldsymbol{x}_0 - \hat{\boldsymbol{x}}_0)\,(\boldsymbol{x}_0 - \hat{\boldsymbol{x}}_0)^T]\,. \tag{47}$$

An integer scaling factor κ is introduced as a tuning parameter for the calculation of the sigma points. For instance, the choice $L + \kappa = 3$ with $L = 2n + m$ is recommended in [23], if the state vector as well as the process and measurement noise can be assumed to be Gaussian. Let us introduce the non-augmented UKF with reduced computational costs by defining $L = n + m$. The weighting factors for $2n + 2m + 1$

sigma points are then given by

$$w_0 = \frac{\kappa}{L + \kappa} \quad \text{and} \quad w_i = \frac{1}{2(L + \kappa)} \quad \text{for} \quad i = 1, \ldots, 2L \ . \tag{48}$$

The scalar factor η, which defines the spread of the sigma points around the mean value, is defined in the form

$$\eta = \sqrt{L + \kappa}. \tag{49}$$

Note that the already discussed choice $L + \kappa = 3$ yields a spread η that is independent of L [23]. Furthermore, let us define the matrices $\boldsymbol{\chi}^w \in \mathbb{R}^{n \times 2n+1}$ and $\boldsymbol{\gamma}^v \in \mathbb{R}^{m \times 2m}$ in the form

$$\boldsymbol{\chi}^w = \left[\mathbf{0}, \ \eta\sqrt{\boldsymbol{Q}}, \ -\eta\sqrt{\boldsymbol{Q}} \right] \quad \text{and} \quad \boldsymbol{\gamma}^v = \left[\eta\sqrt{\boldsymbol{R}}, \ -\eta\sqrt{\boldsymbol{R}} \right] , \tag{50}$$

with $\sqrt{\cdot}$ referring to the matrix square root factorization of the corresponding matrix argument. An efficient way for calculating the square root factorization is given by the Cholesky decomposition.

The following calculations are performed in each sampling interval after the one-short initialization according to (47). The state vectors given by sigma points are arranged in a matrix[1] $\boldsymbol{\chi}^x(k|k) \in \mathbb{R}^{n \times 2n+1}$

$$\boldsymbol{\chi}^x(k|k) = \left[\hat{\boldsymbol{x}}(k|k), \ \hat{\boldsymbol{x}}(k|k) + \eta\sqrt{\boldsymbol{P}_x(k|k)}, \ \hat{\boldsymbol{x}}(k|k) - \eta\sqrt{\boldsymbol{P}_x(k|k)} \right] \tag{51}$$

where the expression $\hat{\boldsymbol{x}}(k|k) \pm \eta\sqrt{\boldsymbol{P}_x(k|k)}$ means that the vector $\hat{\boldsymbol{x}}(k|k)$ is added (subtracted) to each column of the matrix square root factorization of the covariance matrix $\sqrt{\boldsymbol{P}_x(k|k)}$. In a further step, these sigma point vectors are propagated through the nonlinear dynamical system (42) yielding

$$\boldsymbol{\chi}_i^x(k+1|k) = \boldsymbol{f}\Big(\boldsymbol{\chi}_i^x(k|k), \boldsymbol{u}(k)\Big) + \boldsymbol{\chi}_i^w , \tag{52}$$

where $\boldsymbol{\chi}_i^x(k|k)$ and $\boldsymbol{\chi}_i^w, i = 0, \ldots, 2n$ are the column vectors of the matrices $\boldsymbol{\chi}^x(k|k)$ and $\boldsymbol{\chi}^w$, respectively. An extended state sigma points vector $\boldsymbol{\chi}(k+1|k) \in \mathbb{R}^{n \times 2L+1}$ is defined to be used later in the update step

$$\boldsymbol{\chi}(k+1|k) = \left[\boldsymbol{\chi}_i^x(k+1|k), \ \mathbf{0} \right] . \tag{53}$$

The stochastic properties of the random state variables are approximated up to the second order by

$$\hat{\boldsymbol{x}}(k+1|k) = \sum_{i=0}^{2n} w_i \, \boldsymbol{\chi}_i^x(k+1|k), \tag{54}$$

$$\boldsymbol{P}_x(k+1|k) = \sum_{i=0}^{2n} w_i \left(\boldsymbol{\chi}_i^x(k+1|k) - \hat{\boldsymbol{x}}(k+1|k) \right) \left(\boldsymbol{\chi}_i^x(k+1|k) - \hat{\boldsymbol{x}}(k+1|k) \right)^T . \tag{55}$$

Based on these results, the output sigma points are predicted

$$\boldsymbol{\gamma}_i^y(k+1|k) = \boldsymbol{h}\Big(\boldsymbol{\chi}_i^x(k+1|k), \boldsymbol{u}(k+1)\Big), \quad i = 0, \ldots, 2n, \tag{56}$$

---

[1] Here and subsequently, the notation $x(a|b)$ relates to the stochastic properties of a given random variable at the discrete time step a, in which only the measurements of the discrete time steps from 0 to b are incorporated.

The extended output sigma points vector $\boldsymbol{\gamma}(k+1|k) \in \mathbb{R}^{m \times 2L+1}$ takes the measurement noise into account

$$\boldsymbol{\gamma}(k+1|k) = [\,\boldsymbol{\gamma}^y(k+1|k),\, \boldsymbol{\gamma}_0^y(k+1|k) + \boldsymbol{\gamma}^v\,]\ . \tag{57}$$

The predicted stochastic properties of the output vector, cf. (43), are approximated up to the second order in the form

$$\hat{\boldsymbol{y}}(k+1|k) = \sum_{i=0}^{2L} w_i\, \boldsymbol{\gamma}_i(k+1|k), \tag{58}$$

$$\boldsymbol{P}_y(k+1|k) = \sum_{i=0}^{2L} w_i \left(\boldsymbol{\gamma}_i(k+1|k) - \hat{\boldsymbol{y}}(k+1|k) \right) \left(\boldsymbol{\gamma}_i(k+1|k) - \hat{\boldsymbol{y}}(k+1|k) \right)^T . \tag{59}$$

Finally, the Kalman gain matrix is calculated and an estimation update is performed by considering the new measurements $\boldsymbol{y}(k+1)$

$$\boldsymbol{P}_{xy}(k+1|k) = \sum_{i=0}^{2L} w_i \left(\boldsymbol{\chi}_i(k+1|k) - \hat{\boldsymbol{x}}(k+1|k) \right) \left(\boldsymbol{\gamma}_i(k+1|k) - \hat{\boldsymbol{y}}(k+1|k) \right)^T , \tag{60}$$

$$\boldsymbol{K}(k+1) = \boldsymbol{P}_{xy}(k+1|k)\, \boldsymbol{P}_y(k+1|k)^{-1}, \tag{61}$$

$$\hat{\boldsymbol{x}}(k+1|k+1) = \hat{\boldsymbol{x}}(k+1|k) + \boldsymbol{K}(k+1) \left(\boldsymbol{y}(k+1) - \hat{\boldsymbol{y}}(k+1|k) \right), \tag{62}$$

$$\boldsymbol{P}_x(k+1|k+1) = \boldsymbol{P}_x(k+1|k) - \boldsymbol{K}(k+1)\, \boldsymbol{P}_y(k+1|k)\, \boldsymbol{K}(k+1)^T . \tag{63}$$

4   Simulation and experimental studies

First tests of the proposed vehicle state estimation approach were carried out in MATLAB/SIMULINK. In this context, a detailed vehicle model, comprising sub-models for the engine, the powertrain, the hydraulic braking system, the VDC system, the chassis, and the tires, was used to simulate a test vehicle. This model is a development of Robert Bosch GmbH and shows performance comparable to state-of-the-art models available on the market, e.g. CarSim, veDYNA, or CarMaker. The UKF and the classical EKF were implemented as two separate S-Functions allowing for a direct comparison of the estimation results. Thereby, both algorithms were identically parameterized and the sampling time was varied from 5 ms to 40 ms. Noteworthy, there was almost no difference in the estimation performance for sampling times up to 5 ms. A significant difference, however, became apparent with increasing sampling times, see Figure 10. The main reason for this behavior is due to the model linearization in EKF, which entails non-negligible linearization errors at lower vehicle velocities due to (6)–(7), (9)–(10). Thus, extensive simulation studies have shown that the UKF clearly outperforms the EKF in case of larger sampling times.

The performance and robustness of the UKF were tested by means of simulations with varying parameters and different driving situations. The overall results can be qualified as very good. The only parameter which noticeably affects the estimation error was the effective tire radius r_{e}.

Due to the excellent simulation results it was decided to implement the estimation concept in a Conventional BMW 5 Series test vehicle, see Figure 11. The vehicle was additionally equipped with the ADMA[1] measurement unit that allows to precisely capture the longitudinal and lateral vehicle velocities. Different driving maneuvers were performed for testing the estimator performance. The most challenging ones will be presented and discussed in the following.

Figure 12 shows the estimation results for a longitudinal maneuver consisting of acceleration on dry asphalt and ABS braking on a μ-split track. Such μ-split test tracks are very common in the automotive

---

[1] Automotive Dynamic Motion Analyzer (ADMA) is a GPS/INS measurement equipment developed by GeneSys GmbH.
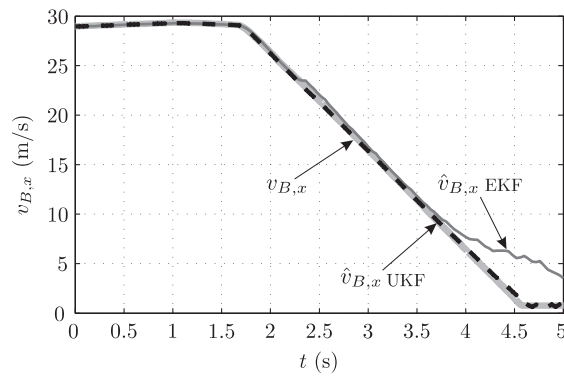
Figure 10. Estimation results for the longitudinal vehicle velocity $v_{B,x}$ in a braking maneuver: Extended Kalman Filter (EKF) and Unscented Kalman Filter (UKF) are identically parameterized for a sampling time of 40 ms.

Figure 11. Conventional BMW 5 Series serves as the test vehicle for the proposed UKF state estimation concept.

industry. They are designed to provide different contact surfaces for left and right vehicle tires. One track surface is commonly covered by dry asphalt and the other by polished ice. The upper plot depicts the four wheel torques M_i, $i \in \{FL, FR, RL, RR\}$ distinguished by means of different line styles. The middle plot presents the measured and the estimated longitudinal velocities, $v_{B,x}$ and $\hat{v}_{B,x}$, as well as the circumferential velocities $r_e \omega_i, i \in FL, FR, RL, RR$ of the individual wheels. The higher slippage of the front right wheel can be explained by the reduced grip conditions on the right vehicle side. The bottom plot shows the internal variable $\mu_{\max}$, which is adapted by the algorithm in order to provide correct estimation results. In summary, the UKF yields reliable and precise estimates $\hat{v}_{B,x}$ of the longitudinal vehicle velocity $v_{B,x}$ during the whole maneuver.

Figure 13 depicts the second longitudinal maneuver. It starts with acceleration on dry asphalt and finishes with braking on a surface with areas consisting of dry asphalt and ice. The selection and the layout of the presented signals are equal to the previous figure. Particularly remarkable is the outstanding estimation performance in situations with changing road conditions, e.g., at 20.5 s and 31.5 s. The quick switching from acceleration to braking at 29.7 s is handled properly as well. A detailed view of this maneuver is shown in Figure 14. By considering the bottom plot it becomes apparent that the internal variable $\mu_{\max}$ has relatively slow dynamics and therefore only provides rough information about the actual grip conditions. However, this is not really a drawback since we are primarily interested in an accurate and robust estimation of the longitudinal and lateral vehicle velocities.

For lateral dynamics tests the Increasing Sine Steer (ISS) maneuver was chosen. It is realized by means of a steering machine so that the steering angle follows a predefined sine function with increasing amplitude. Figure 15 shows the estimation results for the ISS maneuver performed on dry asphalt. The average
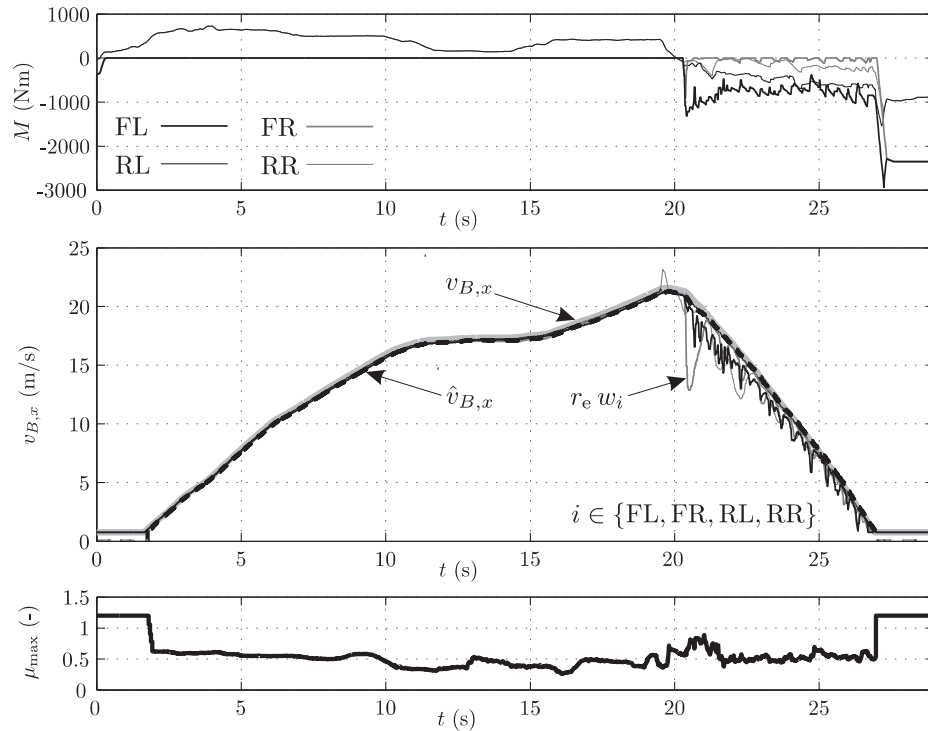
Figure 12. Estimation results for a longitudinal maneuver. Acceleration on dry asphalt is followed by ABS braking on μ-split surface.
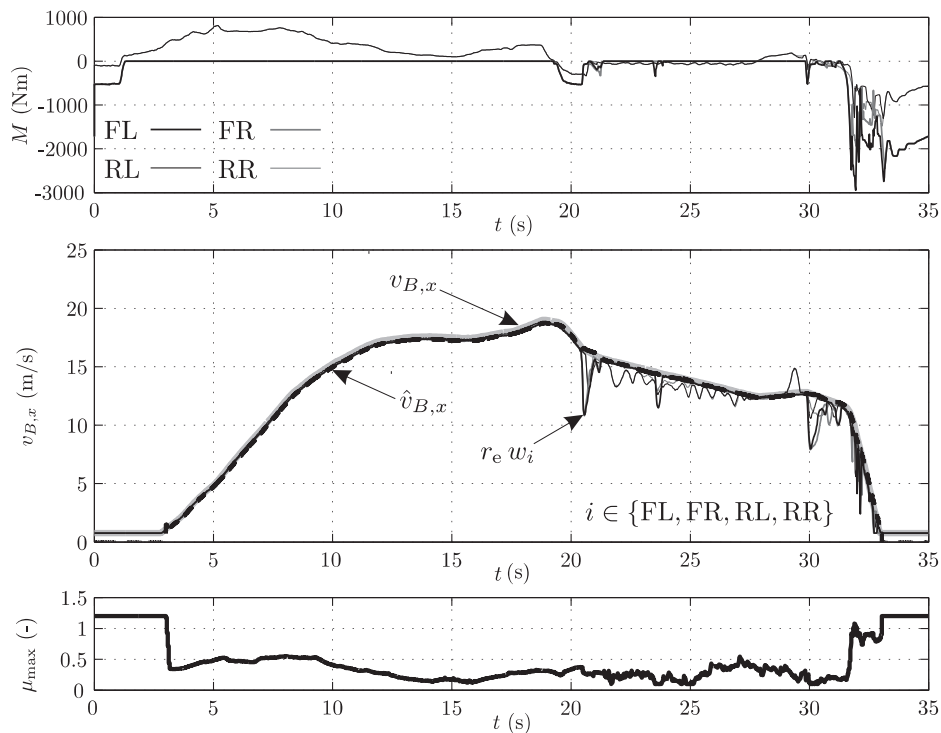

Figure 13.   Estimation results for a longitudinal maneuver. Acceleration on dry asphalt followed by braking on a surface with areas consisting of dry asphalt and ice.
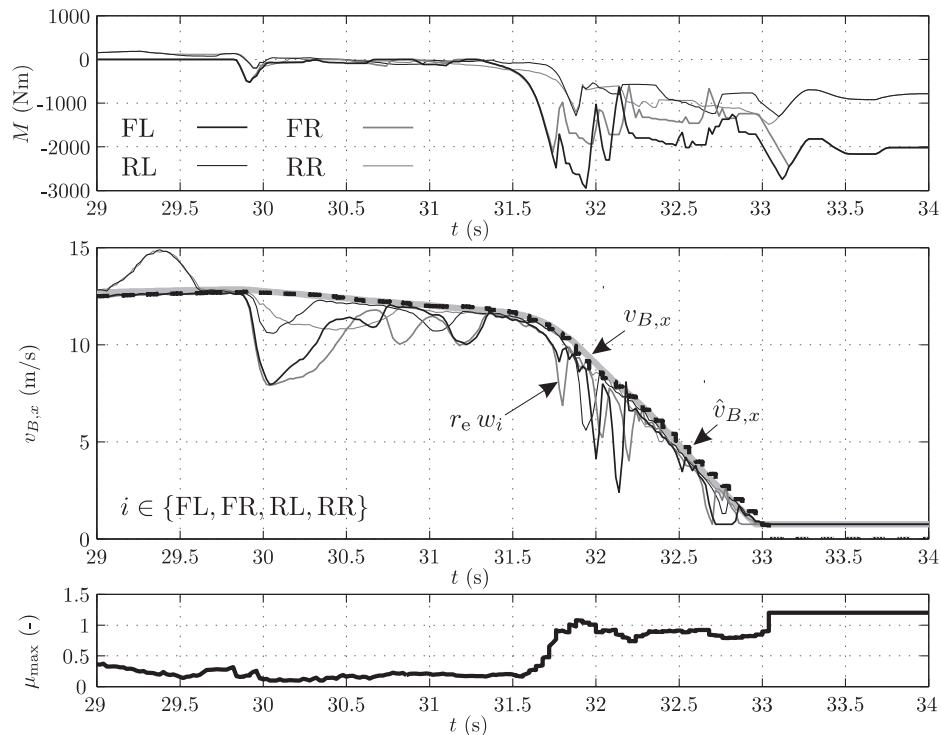
Figure 14. Detailed view of the longitudinal maneuver from Figure 13. This part of the maneuver depicts ABS braking on a surface with changing friction coefficients.

steer angle of the front wheels is denoted by $\delta_f = (\delta_{FL} + \delta_{FR})/2$. The aggressive steering input at 100 km/h brought the vehicle close to it's physical limits. This is why the vehicle dynamics control system triggered active braking interventions as can be seen in the time evolutions of the wheel torques $M_i, i \in \{FL, FR, RL, RR\}$ in the upper right plot of Figure 15. The estimation results for the longitudinal and the lateral velocities, $\hat{v}_{B,x}$ and $\hat{v}_{B,y}$, are very good despite this challenging dynamical testing maneuver.

To give some insight into the robustness properties of the developed concept, the ISS maneuver was additionally performed under strongly varying conditions. Figure 16 depicts the estimation results for an ISS maneuver where the vehicle has summer tires at the front axle and winter tires at the rear axle. This combination massively changes the vehicle behavior towards strong oversteering and provokes exceptional driving situations. The vehicle only remained controllable at modest velocities supported by very strong braking interventions of the vehicle dynamics control. Figure 17 shows another interesting experiment. Here, the ISS maneuver is performed on an ice track with low grip conditions resulting in extreme driving dynamics. During both test maneuvers, the handling dynamics of the vehicle has changed dramatically, so that the default parametrization of the vehicle model was far from the reality. Nevertheless, the estimates of the longitudinal and the lateral velocities, $\hat{v}_{B,x}$ and $\hat{v}_{B,y}$, perfectly match the real time evolutions $v_{B,x}$ and $v_{B,y}$.

5 Conclusion

In this contribution, a new approach for the accurate vehicle state estimation based on a detailed vehicle model and an Unscented Kalman Filter (UKF) was presented. The mathematical model relies on a planar two-track model extended by an advanced vertical tire force calculation and a simplified version of the empirical Magic Formula. For the UKF design the time discretization of the nonlinear mathematical model was performed by means of a Lie-Taylor series approach. The classical augmented UKF realization was reformulated for the case of the additive process and measurement noises providing beneficial reduction of computational costs. The performance and robustness of the developed vehicle state estimator were
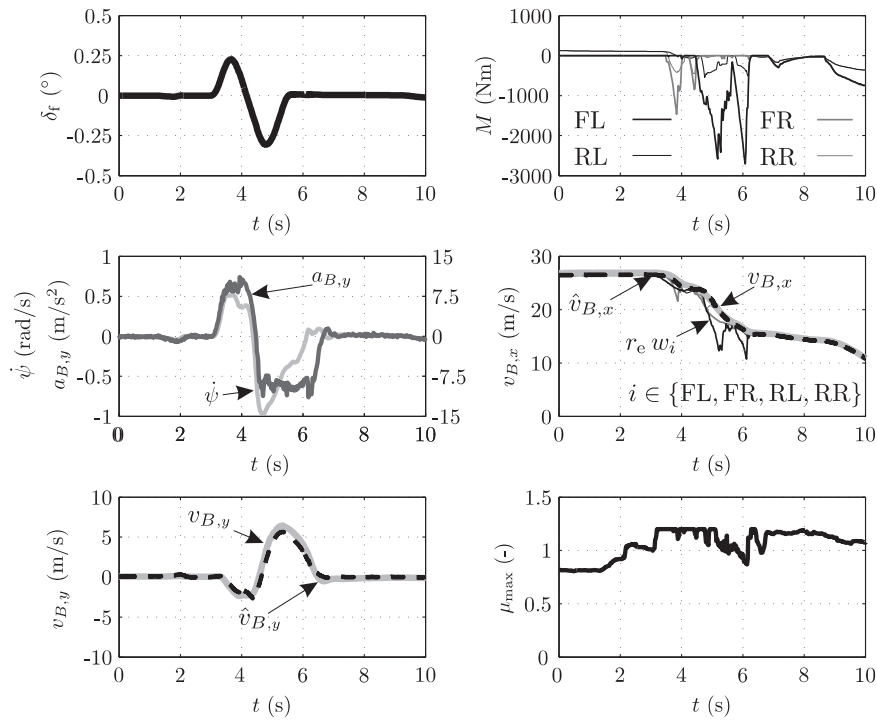
Figure 15. Estimation results for an increasing sine steer maneuver performed on dry asphalt.
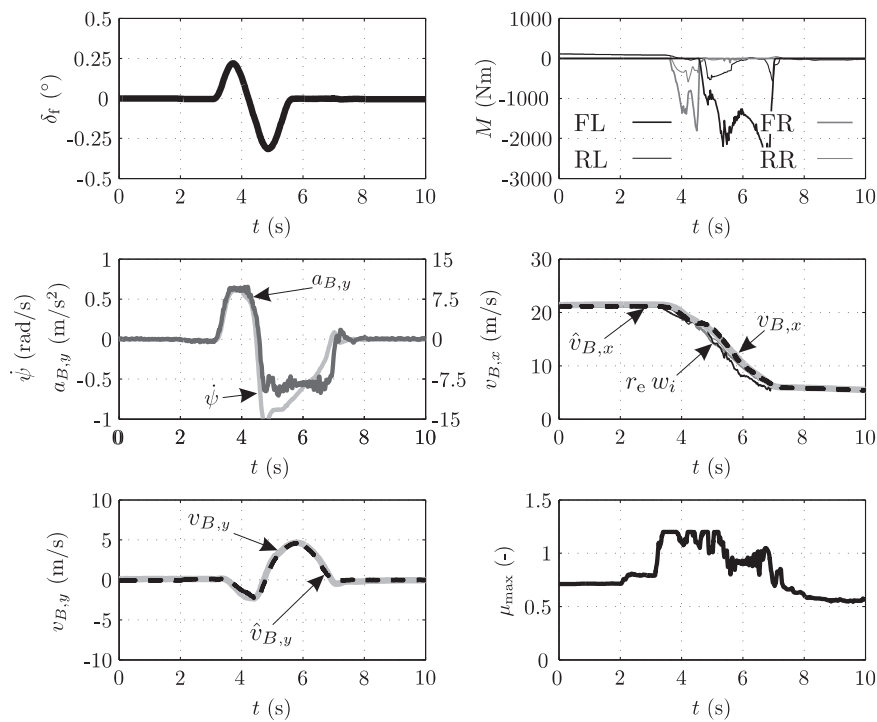

Figure 16.   Estimation results for an increasing sine steer maneuver performed on dry asphalt. Summer tires are mounted at the front axle and winter tires at the rear axle, respectively.
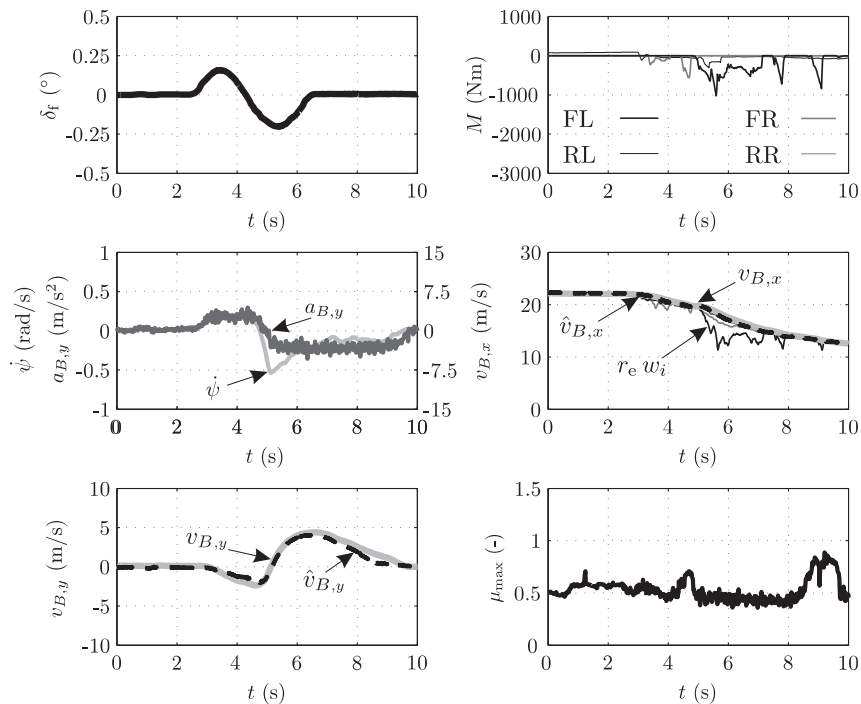
Figure 17. Estimation results for an increasing sine steer maneuver performed on an ice track.

extensively tested in numerous simulation studies and in a conventional BMW 5 Series test vehicle. To sum it up, the UKF outperforms the standard Extended Kalman Filter (EKF) approach in particular in case of larger sampling times, mainly due to the inherent incorporation of the system's nonlinearities in the design process. Thus, the UKF turns out to constitute a good compromise between accuracy, robustness and computational costs. Future research will deal with the consideration of the road slope and the road banking in the vehicle estimator design.

Acknowledgment

References

[1] van Zanten, A., Erhardt, R., and Pfaff, G., FDR — Die Fahrdynamikregelung von Bosch, *ATZ Automobiltechnische Zeitschrift*, vol. 96, no. 11, pp. 674–689, 1994.
[2] Lie, A., Tingvall, C., Krafft, M., and Kullgren, A., The Effectiveness of ESC (Electronic Stability Control) in Reducing Real Life Crashes and Injuries, *Proc. of the Int. Techn. Conf. on the Enhanced Safety of Vehicles (ESV)*, no. 05-0135, June 2005, Washington D.C., USA.
[3] Farmer, C.M., *Effects of Electronic Stability Control: An Update*, Insurance Institute for Highway Safety, May 2006, Arlington, USA.
[4] Fukada, Y., Slip-Angle Estimation for Vehicle Stability Control, *Vehicle System Dynamics*, vol. 32, no. 4–5, pp. 375–388, 1999.
[5] Hac, A., and Melinda, D.S., Estimation of Vehicle Side Slip Angle and Yaw Rate, *SAE Technical Paper Series*, no. 2000-01-0696, 2000.
[6] Huang, P., Smakman, H., and Guldner, J., Design of a Vehicle State Observer for Vehicle Dynamics Control Systems, *Proc. of the Int. Symp. on Advanced Vehicle Control (AVEC)*, pp. 449–452, August 2000, Ann Arbor, Michigan, USA.
[7] Shim, T., and Margolis, D., Model-Based Road Friction Estimation, *Vehicle System Dynamics*, vol. 41, no. 4, pp. 249–276, 2004.
[8] Canudas-de-Wit, C., and Horowitz, R., Observers for Tire/Road Contact Friction using only Angular Velocity Information, *Proc. of the IEEE Conf. on Decision & Control*, pp. 3932–3937, December 1999, Phoenix, Arizona, USA.

[9] Canudas-de-Wit, C., Petersen, M.L., and Shiriaev, A., A new Nonlinear Observer for Tire/Road Distributed Contact Friction, *Proc. of the IEEE Conf. on Decision & Control*, pp. 2246–2251, December 2003, Maui, Hawaii, USA.

[10] Hiemer, M., von Vietinghoff, A., Kiencke, U., and Matsunaga, T., Determination of the Vehicle Body Side Slip Angle with Non-Linear Observer Strategies, *SAE Technical Paper Series*, no. 2005-01-0400, 2005.

[11] Imsland, L., Johansen, T.A., Fossen, T.I., Kalkkuhl, J.C., and Suissa, A., Vehicle Velocity Estimation using Modular Nonlinear Observers, *Proc. of the IEEE Conf. on Decision & Control*, pp. 6728–6733, December 2005, Seville, Spain.

[12] Kobayashi, K., Cheok, K.C., and Watanabe, K., Estimation of Absolute Vehicle Speed using Fuzzy Logic Rule-Based Kalman Filter, *Proc. of the American Control Conf.*, pp. 3086–3090, June 1995, Seattle, Washington, USA.

[13] Daiß, and A., Kiencke, U., Estimation of Vehicle Speed: Fuzzy-Estimation in Comparison with Kalman-Filtering, *Proc. of the IEEE Conf. on Control Application*, pp. 281–284, September 1995, Albany, New York, USA.

[14] Ray, L.R., Nonlinear State and Tire Force Estimation for Advanced Vehicle Control, *IEEE Trans. on Control Systems Technology*, vol. 3, no. 1, pp. 117–124, 1995.

[15] Best, M.C., and Gordon T.J., Real-Time State Estimation of Vehicle Handling Dynamics Using an Adaptive Kalman Filter. *Proc. of the Int. Symp. on Advanced Vehicle Control (AVEC)*, pp. 183–188, September 1998, Nagoya, Japan.

[16] Venhovens P.J.Th., and Naab, K., Vehicle Dynamics Estimation Using Kalman Filters, *Vehicle System Dynamics*, vol. 32, **no.??** pp. 171–184, 1999.

[17] Samadi., B., Kazemi, R., Nikraversh, K.Y., and Mansour, K., Real-Time Estimation of Vehicle State and Tire-Road Friction Forces, *Proc. of the American Control Conf.*, pp. 3318–3323, June 2001, Arlington, Virginia, USA.

[18] Satria, M., and Best, M.C., Comparison between Kalman Filter and Robust Filter for Vehicle Handling Dynamics State Estimation, *SAE Technical Paper Series*, no. 2005-01-11850, 2005.

[19] Zuurbier, J., and Bremmer, P., State Estimation for Integrated Vehicle Dynamics Control, *Proc. of the Int. Symp. on Advanced Vehicle Control (AVEC)*, pp. 183–188, September 2002, Hiroshima, Japan.

[20] von Vietinghoff, A., Feist, A., and Hiemer, M., Extended Kalman-Bucy Filter Design for Improved Lateral Vehicle Dynamics Description, *Reports on Industrial Information Technology*, vol. 8, pp. 37–46, Shaker Verlag, Aachen, 2005.

[21] Wenzel, T.A., Burnham, K.J., Blundell, M.V., and Williams, R.A., Dual Extended Kalman Filter for Vehicle State and Parameter Estimation, *Vehicle System Dynamics*, vol. 44, no. 2, pp. 153–171, 2006.

[22] Pengov, M., d'Andréa-Novel, B., Fenaux, E., Grazi, S., and Zarka, F., A Comparison Study of Two Kinds of Observers for a Vehicle, *Proc. of the European Control Conf.*, pp. 1068–1073, September 2001, Porto, Portugal.

[23] Julier, S.J., Uhlmann, J.K., and Durrant-Whyte, H.F., A New Approach for Filtering Nonlinear Systems, *Proc. of the American Control Conf.*, pp. 1628–1632, June 1995, Seattle, Washington, USA.

[24] van der Merwe, R., Wan E.A., and Julier, S.I., Sigma-Point Kalman Filters for Nonlinear Estimation and Sensor-Fusion - Applications to Integrated Navigation, *Proc. of the AIAA Guidance, Navigation & Control Conf. (GNC)*, AIAA-2004-5120, August 2004, Providence, Rhode Island.

[25] Mitschke, M., and Wallentowitz, H., *Dynamik der Kraftfahrzeuge*, 4th edition, Springer, Berlin Heidelberg, 2004.

[26] Pacejka, H.B., *Tyre and Vehicle Dynamics*, Elsevier Butterworth-Heinemann, Oxford, 2002.

[27] Bakker, E., Nyborg, L., and Pacejka, H.B., Tyre Modelling for Use in Vehicle Dynamics Studies, *SAE Technical Paper Series*, no. 870421, 1987.

[28] Kazantis, N., and Kravaris, C., System-theoretic Properties of Sampled-data Representations of Nonlinear Systems obtained via Taylor-Lie Series, *Int. J. Control*, vol. 67, no. 6, pp. 997–1020, 1997.

[29] Kalman, R.E., A New Approach to Linear Filtering and Prediction Problems, *Transactions of the ASME-Journal of Basic Engineering*, vol. 82, series D, pp. 35–45, 1960.

[30] Bar-Shalom, Y., Li, X.-R., and Kirubarajan, T., *Estimation with Applications to Tracking and Control*, John Wiley & Sons, Inc., USA, 2001.